Coherent Ultrafast Stimulated X-Ray Raman Spectroscopy of Dissipative Conical Intersections

Florian Otterpohl,[1,*] Daniel Keefer,[2] Shaul Mukamel,[3] and Michael Thorwart[1,4]
[1]I. Institut für Theoretische Physik, Universität Hamburg, Notkestraße 9, 22607 Hamburg, Germany
[2]Max-Planck-Institut für Polymerforschung, 55128 Mainz, Germany
[3]Department of Chemistry, University of California, Irvine, Irvine, California 92614, USA
[4]The Hamburg Center for Ultrafast Imaging, Luruper Chaussee 149, 22761 Hamburg, Germany

(Received 24 January 2024; accepted 25 July 2024; published 28 August 2024)

The quantum coherent dynamics of a vibronic wave packet in a molecule passing through a conical intersection can be revealed using attosecond transient coherent Raman spectroscopy. In particular, the time evolution of the electronic coherence can be monitored in the presence of vibrational dynamics. So far, the technique has been investigated without including environmental quantum noise. Here, we employ the numerically exact hierarchy equation of motion approach to show that the transient coherent Raman signals are robust and accessible on times of up to a few hundred femtoseconds with respect to electonic and vibrational dephasing.

DOI: 10.1103/PhysRevLett.133.098001

Introduction—Conical intersections are crucial in photochemical processes of polyatomic molecules [1–4]. They appear when two or more electronic potential energy surfaces become degenerate. Then, electronic and nuclear motions take place on similar timescales and thus become strongly coupled due to the breakdown of the Born-Oppenheimer approximation that usually allows for their separate treatment. Molecular funnels promote radiationless transitions between electronic states in nonadiabatic processes which are crucial for numerous processes, including photoisomerization [2,5], photosynthesis [6], and the photostability of DNA [2].

Electronic transitions at a conical intersection typically occur on the femtosecond timescale and involve a broad range of vibronic energies in a confined nuclear space. While attosecond transient absorption spectroscopy can provide strong evidence of conical intersections through rapid change or emergence of absorption lines [7,8], features emerging directly at the conical intersection, like vibronic coherences, have not yet been observed directly. Recently, a hybrid qubit-oscillator circuit quantum electrodynamics simulator of an artificial conical intersection has demonstrated branching between different photochemical reaction products with strong dissipation [9]. Moreover, a trapped-ion quantum simulator has been designed in which both the ion's electronic and motional degrees of freedom engineer a Jahn-Teller Hamiltonian, with the dynamics occurring on the millisecond timescale [10]. Yet, a direct observation of the coherent wave packet dynamics around conical intersections, let alone the time-resolved measurement of electronic or vibronic coherences around the diabatic point so far remains elusive.

Advanced theoretical concepts for monitoring the dynamics around a conical intersection have also been proposed using optical spectroscopy of the vibrational wave packet (as an indirect measure) [11] or the time-resolved x-ray absorption or photoelectron spectroscopy [12]. A versatile, recently proposed technique exploits the transient redistribution of ultrafast electronic coherences in attosecond Raman signals (TRUECARS) [13–16]. It directly reveals the time-dependent emergent vibronic coherences of the wave packet around a conical intersection [13,17] via a stimulated coherent Raman process. Upon optical excitation, the combination of a broadband and a narrow-band x-ray pulse permits both sufficient spectral and temporal resolution. Since the two x-ray pulses are chosen to be off-resonant from the molecular core states, the signal is not influenced by electronic population dynamics and thus provides a background-free measure of coherences. While experimentally challenging, in particular due to the required precise phase control between both x-ray pulses, recent developments in free electron lasers have brought an implementation of TRUECARS into potential reach.

So far, TRUECARS has been implemented for closed molecular quantum systems. A more realistic picture needs to include the coupling to fluctuations stemming from a large number of environmental degrees of freedom [18–21]. In particular, for conical intersections, electronic coherence may be disturbed by two sources of noise. First, the direct coupling of the electronic states to fluctuating charges in the molecular host and the solvent (electronic bath) gives rise to electronic dephasing and

*Contact author: florian.otterpohl@physik.uni-hamburg.de

damping. In addition, the nuclear modes participating in the conical intersection are also damped by other fluctuating nuclear degrees of freedom of the molecular host or the solvent. Via the coupling of the electron to these damped nuclear modes, this vibrational bath generates additional damping of the electronic coherence. In general, in molecular systems, direct electronic damping is rather strong and occurs on timescales of about 100 fs [22–27]. On the other hand, vibrational damping of the vibrational modes is much weaker and arises on timescales of a few ps [22–27].

In this study, we compute TRUECARS in a model system of two molecular electronic states with two vibrational modes which form a bimodal conical intersection. The electronic states are coupled directly to an electronic bath, while the two vibrational modes are coupled to their vibrational baths. The latter affects electronic coherence via the vibronic coupling [22–27]. The electronic and the vibrational baths are described within the formalism of quantum dissipative systems in terms of harmonic environments with a bilinear coupling to the electronic or vibrational degrees of freedom. The two vibrational modes participating in the conical intersection (known as the coupling and the tuning mode) are then transformed as part of the harmonic environment, yielding an effective spin-boson model with two noncommuting structured vibrational baths and an electronic bath. We analyze the nonequilibrium quantum dynamics using the numerically exact hierarchy equation of motion [28]. We find that the signal is robust against realistic environmental disturbances and that it is indeed measurable on the few hundred femtosecond timescale even in the presence of a dissipative environment.

Model—We consider the Hamiltonian ($\hbar = 1$) $H = H_{\mathrm{el}} + H_{\text{el-nuc}} + H_{\mathrm{nuc}} + H_{\mathrm{env}}$, consisting of a molecular electronic two-level Hamiltonian

$$H_{\mathrm{el}} = \frac{\epsilon}{2}\sigma_z + \frac{\Delta}{2}\sigma_x, \tag{1}$$

with the Pauli matrices $\sigma_{x/z}$, the energy bias ϵ, and the coupling Δ. The electronic sector is bilinearly coupled to two nuclear modes with the Hamiltonian $H_{\mathrm{nuc}} = \sum_{i\in\{c,t\}} \Omega(P_i^2 + Q_i^2)/2$, with the corresponding position and momentum operators P_i and Q_i of the tuning (t) and the coupling (c) mode, assuming for simplicity that both have identical vibrational frequencies Ω. The vibronic coupling is described by the Hamiltonian $H_{\text{el-nuc}} = \kappa_c\sigma_x Q_c + \kappa_t\sigma_z Q_t$, with the vibronic coupling constants $\kappa_{c/t}$.

To be specific and assuming a typical molecular system, we employ the model parameters [19,20,22–27] $\epsilon = \Omega = 300\ \mathrm{cm}^{-1}(\approx 37.2\ \mathrm{meV})$, $\Delta = 50\ \mathrm{cm}^{-1}(\approx 6.2\ \mathrm{meV})$, $\kappa_t = 150\ \mathrm{cm}^{-1}(\approx 18.6\ \mathrm{meV})$, and $\kappa_c = 75\ \mathrm{cm}^{-1}(\approx 9.3\ \mathrm{meV})$. The corresponding potential energy surfaces exhibit a conical intersection as shown in Fig. 1. The parameter choice also mimics typical molecular systems with Jahn-Teller distortions, such as halobenzene cations, triazine, or metal trimers, such as Cu_3, or Li_3, Na_3, Mn_3, or triptycene, see Table VII of Ref. [29].

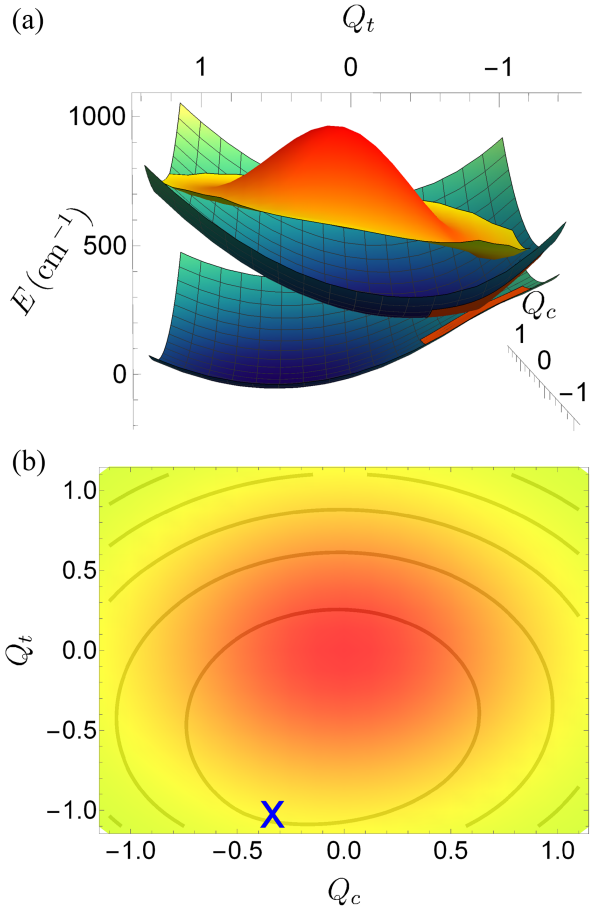

FIG. 1. (a) Potential energy surfaces of $H_{\mathrm{el}} + H_{\text{el-nuc}} + H_{\mathrm{nuc}}$ and probability density of the initial state based on the provided parameters. The region around the conical intersections is highlighted in orange. (b) The potential energy surface is depicted with contour lines, and the initial state's probability density is color coded. The conical intersection is highlighted by a blue cross.

To describe environmental effects, the molecular degrees of freedom are coupled to a dissipative environment with the Hamiltonian

$$H_{\mathrm{env}} = \sum_{i\in\{c,t,el\}} \sum_{\alpha} [c_\alpha^{(i)} A_i (a_\alpha^{(i)} + a_\alpha^{(i)\dagger}) + \omega_\alpha^{(i)} a_\alpha^{(i)\dagger} a_\alpha^{(i)}]. \tag{2}$$

We model the effect of vibrational damping of the tuning (t) and the coupling (c) mode and of electronic dephasing (el) via the operators $A_c = Q_c$, $A_t = Q_t$, and $A_{\mathrm{el}} = \sigma_z$, respectively. The respective bath counterterms are included as usual [18–21], but not explicitly written here. The harmonic oscillator baths are characterized by their spectral densities $J_i(\omega) = \pi \sum_\alpha (c_\alpha^{(i)})^2 \delta(\omega - \omega_\alpha^{(i)})$. We assume for the vibrational damping pure Ohmic spectral densities with equal damping constants η_{vib} for both modes, i.e., $J_{(c,t)}(\omega) = \eta_{\mathrm{vib}}\omega$. This form corresponds to a frequency-independent

vibrational Stokes damping force [19,20]. For the electronic bath, we also assume an Ohmic form $J_{\rm el}(\omega) = \eta_{\rm el}\omega\gamma^2/(\gamma^2+\omega^2)$, where $\eta_{\rm el}$ is the electronic damping constant and the Debye cut-off frequency is fixed to $\gamma = 4\epsilon$ throughout this work. This Debye form is known to properly describe electronic dephasing for typical molecular systems [19,20,24–27]. It is, e.g., related to the dielectric function $\varepsilon(\omega)$ of a solvent via $J_{\rm el}(\omega) \propto \mathrm{Im}\ 1/\varepsilon(\omega)$. To describe electronic dephasing occurring on the timescale of 100 fs, we choose below $\eta_{\rm el}$ in the range of 0.1. The vibrational relaxation occurs on the ps timescale which is taken into account by setting $\eta_{\rm vib}$ in the range of 0.01.

The TRUECARS technique uses a combination of a broadband pulse $\mathcal{E}_0(t)$ and a narrow-band pulse $\mathcal{E}_1(t)$ as a probing field, with $H_{\rm spec}(t) = \sigma_x|\mathcal{E}_0(t)+\mathcal{E}_1(t)|^2$, and Gaussian field envelopes $\mathcal{E}_{0/1}(t) = \exp(-t^2/2\sigma_{0/1}^2)/\sigma_{0/1}$, with the pulse durations $\sigma_0 = 7.5$ fs and $\sigma_1 = 30$ fs. By this, we ensure the required combination of a broadband and a narrow-band x-ray pulse [13]. Specifically, σ_1 must be significantly shorter than the timescale of the electronic dynamics and yet spectrally narrower than the electronic energy bias, while σ_0 constitutes an envelope function on the TRUECARS and is thus chosen to be sufficiently small. The electronic dipole operator σ_x describes the Raman transitions between the electronic states. We do not include competing photoionization processes in the simulations. The TRUECARS [13] then becomes

$$S(\omega,T) = 2\Re\int_{-\infty}^{\infty} \mathrm{d}t e^{i\omega(t-T)}\mathcal{E}_0^*(\omega)\mathcal{E}_1(t-T)\langle\sigma_x(t)\rangle \qquad (3)$$

for a given Raman frequency ω and a delay time T.

Mapping to an effective spin-boson model—To obtain the dissipative wave packet dynamics, we map the Hamiltonian to an effective spin-boson model with a nontrivial environmental spectral density. To that end, we follow the procedure of Refs. [22,23,32] and include both the nuclear tuning and the coupling modes as part of the environment such that the Hamiltonian becomes $H = H_{\rm el} + H_{\rm env}^{\rm eff}$, where $H_{\rm env}^{\rm eff}$ is formally identical to Eq. (2), but with $A_c = \sigma_x$ and $A_t = \sigma_z$ and with the effective spectral densities

$$J_{c/t}^{\rm eff}(\omega) = \frac{16\eta_{\rm vib}\kappa_{c/t}^2\omega\Omega^2}{(\Omega^2-\omega^2)^2 + (2\pi\eta_{\rm vib}\omega\Omega)^2}. \qquad (4)$$

We thus obtain an effective spin-boson model in which the electronic two-level system couples to two harmonic baths, each with a pronounced peak at the mode frequency Ω, whose width is determined by $\eta_{\rm vib}$. The baths couple to two noncommuting electronic operators. The mapping is exact, yet it is based on the assumption that both the tuning and coupling modes are initially in a thermal equilibrium (mixed) state. This is different from the initial preparation used in Refs. [13,17] for the nondissipative TRUECARS.

The electronic two-state system is initially prepared in the excited electronic state and all harmonic degrees of freedom are initialized at thermal equilibrium at room temperature (293 K).

The structured environment coupled to the electronic system induces non-Markovian dynamics. The resulting bath autocorrelation function shows damped oscillatory dynamics in time, with the oscillation frequency Ω and the decay determined by $\eta_{\rm vib}$. To obtain the dissipative wave packet dynamics, we shall use the numerically exact method of the hierarchical equations of motion [28] as implemented in the QuTiP library [30,31]. It is ideally suited for the Drude-Ohmic type of spectral densities used here. We thus obtain $\langle\sigma_x(t)\rangle$.

Dissipative TRUECARS—The signals $S(\omega,T)$ of the undamped (a) and the damped (b) system are shown in Fig. 2. For the latter, we set $\eta_{\rm el} = 0.1$ and $\eta_{\rm vib} = 0.01$,

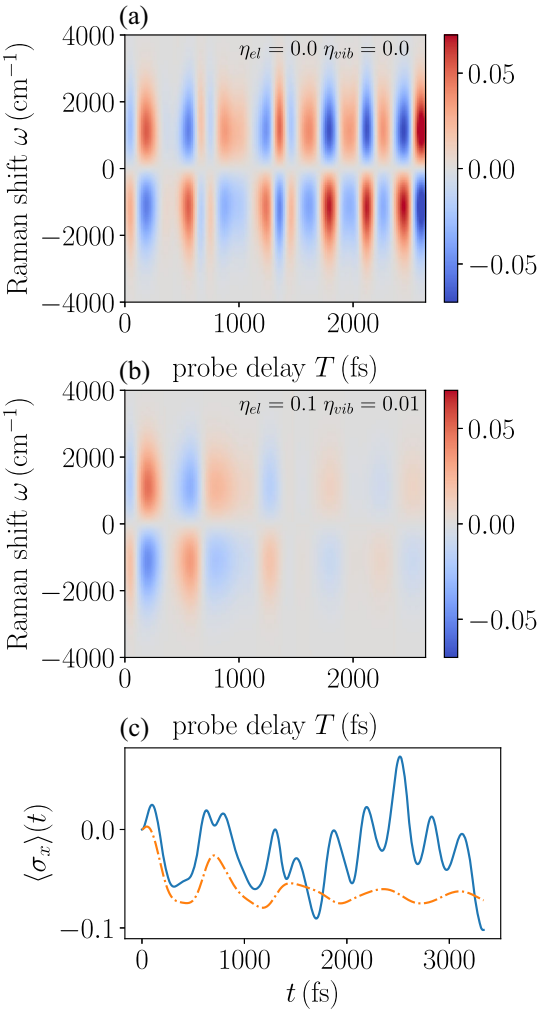

FIG. 2. TRUECARS $S(\omega,T)$, Eq. (3), for (a) the case without damping ($\eta_{\rm el} = 0 = \eta_{\rm vib}$), and (b) the case with damping ($\eta_{\rm el} = 0.1$, $\eta_{\rm vib} = 0.01$). (c) Time evolution of $\langle\sigma_x(t)\rangle$. The solid line represents the undamped case, while the dash-dotted line represents the damped case.

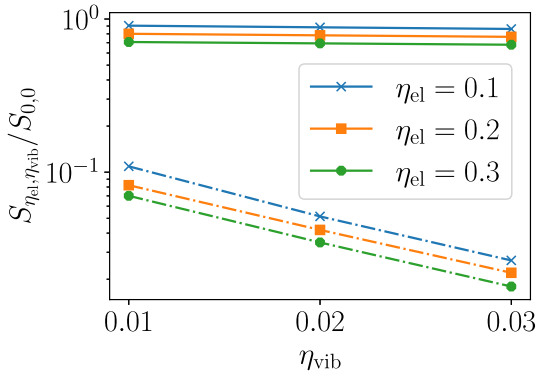

FIG. 3. Ratio of the magnitudes of the local maxima of the damped TRUECARS $S_{\eta_{\rm el},\eta_{\rm vib}}(\omega = 0.12\ \text{eV}, T)$ and the corresponding undamped signal $S_{0,0}(\omega = 0.12\ \text{eV}, T)$ for all $(\eta_{\rm el}, \eta_{\rm vib}) \in \{0.1, 0.2, 0.3\} \times \{0.01, 0.02, 0.03\}$. The solid lines represent the local maxima closest to $T = 200$ fs, while the dash-dotted lines indicate the maxima closest to $T = 2200$ fs.

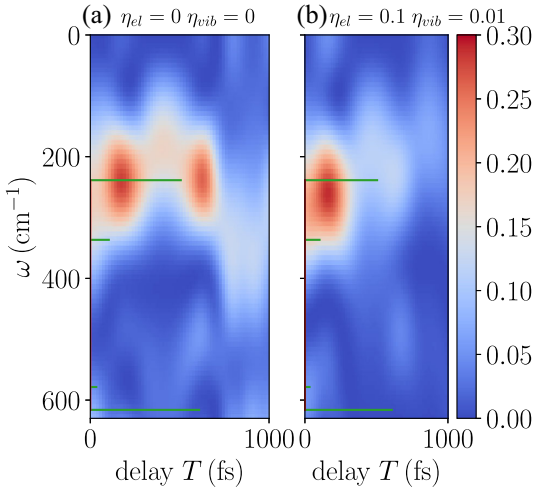

FIG. 4. FROG Signal $I(\omega, T)$, Eq. (5), with $S(t) = S(\omega = 1.2\ \text{eV}, T)$ for (a) the undamped case ($\eta_{\rm el} = 0 = \eta_{\rm vib}$), and (b) the damped case $\eta_{\rm el} = 0.1, \eta_{\rm vib} = 0.01$. The green bars mark the stick spectrum of the undamped vibronic Hamiltonian.

reflecting the fact that electronic damping is much faster than vibrational damping [24–27].

The red and blue signals show the Stokes and the anti-Stokes components of the Raman spectra. The oscillatory pattern for increasing delay time T indicates that the electronic coherence lifetime is longer than the time window T and exceeds 2 ps in the absence of dissipation. The oscillatory pattern in the undamped case becomes more complex at longer delay times, since after the first passage of the conical intersection, the electronic wave packet returns and repasses through the intersection, thereby generating new electronic coherences on a timescale determined by the vibrational frequency.

In the presence of dissipation, the oscillatory pattern fades out with T on a timescale of a few hundred femtoseconds. Nevertheless, although being fragile against environmental noise, the electronic coherences are still observable.

To quantify the extinction of electronic coherence, we consider the ratio of the TRUECARS strength with and without damping for fixed delay times. In Fig. 3, we show the ratio $S_{\eta_{\rm el},\eta_{\rm vib}}/S_{0,0}$, in which we take the local maxima at those waiting times closest to the two different values $T = 200$ fs (solid lines) and $T = 2200$ fs (dashed-dotted lines). At short waiting times $T = 200$ fs, the TRUECARS is still sizable even for rather strong electronic damping. At these short times, the weaker vibrational damping has essentially no effect. This, however, sets in at longer waiting times, as can be seen from the data for $T = 2200$ fs. The signal, though being an order of magnitude weaker, is, however, still observable, even for increased electronic damping. This clearly shows that TRUECARS is a versatile tool to uncover time-dependent electronic coherences in the dynamics of an electronic wave packet in the vicinity of a conical intersection even in the presence of electronic and vibrational damping.

The fate of the coherences in the vicinity of the conical intersection may also be revealed by the frequency-resolved optical gating (FROG) spectrogram [33]

$$I(\omega, T) = \left| \int_{-\infty}^{\infty} \mathrm{d}t\, S(t) E_{\rm gate}(t - T) e^{-i\omega t} \right|^2, \qquad (5)$$

with the gating function $E_{\rm gate}(t - T) = 1$ if $0 \le t - T \le 1000$ fs and $E_{\rm gate}(t - T) = 0$ else. In Fig. 4, the FROG signal $I(\omega, T)$ of the undamped case is compared to the damped case. We observe that a strong FROG component develops around 250 cm^{-1}, which corresponds to the fundamental energy gap between the vibronic states, as indicated by the stick spectrum (green bars in Fig. 4). The stick spectrum is further detailed in the Supplemental Material [34]. The signal weakens with increasing T, moves to smaller frequencies and reappears again around 250 cm^{-1}, before it disappears eventually. In the presence of damping, the FROG signal emerges at slightly higher frequencies, approximately around 270 cm^{-1}, due to the bath-induced Stokes shift. Although the FROG signal diminishes within a delay time window of about 300 fs, it remains observable during this period.

Conclusions—We have shown that the vibronic coherences of an electronic wave packet, which develop during its passage through a conical intersection, can be reliably revealed even in the presence of realistically strong electronic dephasing and vibrational damping. The TRUECARS of the damped systems decays on typical timescales of a few hundred femtoseconds and is thus still long-lived enough to be measurable in a spectroscopic experiment at room temperature. A FROG-type postprocessing analysis reliably captures the frequency distribution of the vibronic coherence emerging at the conical

intersection also in the damped system. This finding is encouraging to experimentalists and is likely to survive even when a stochastic train of pump and probe pulses is applied [35]. Potential implications of the observed electronic and vibrational coherence as a resource for applications in molecular electronics, optoelectronics, and quantum information processing are foreseeable, e.g., by increasing the efficiency of optoelectronic devices by accelerating and controlling the involved short-time dynamics [36] or by tailoring the nonradiative decay pathways in solid-state luminescent organic molecular crystals [37].

Acknowledgments—We gratefully acknowledge support from the Cluster of Excellence "Advanced Imaging of Matter" EXC 2056 (390715994). S. M. gratefully acknowledges support of the NSF through Grant No. CHE-2246379.

[1] D. R. Yarkony, Diabolical conical intersections, Rev. Mod. Phys. **68**, 985 (1996).
[2] W. Domcke, D. R. Yarkony, and H. Köppel, *Conical Intersections: Electronic Structure, Dynamics and Spectroscopy* (World Scientific, Singapore, 2004).
[3] W. Domcke, H. Köppel, and D. R. Yarkony, *Conical Intersections: Theory, Computation and Experiment* (World Scientific, Singapore, 2011).
[4] W. Domcke and D. R. Yarkony, Role of conical intersections in molecular spectroscopy and photoinduced chemical dynamics, Annu. Rev. Phys. Chem. **63**, 325 (2012).
[5] D. Polli *et al.*, Conical intersection dynamics of the primary photoisomerization event in vision, Nature (London) **467**, 440 (2010).
[6] G. Olaso-González, M. Merchán, and L. Serrano-Andrés, Ultrafast electron transfer in photosynthesis: Reduced pheophytin and quinone interaction mediated by conical intersections, J. Phys. Chem. B **110**, 24734 (2006).
[7] K. F. Chang, M. Reduzzi, H. Wang, S. M. Poullain, Y. Kobayashi, L. Barreau, D. Prendergast, D. M. Neumark, and S. R. Leone, Revealing electronic state-switching at conical intersections in alkyl iodides by ultrafast XUV transient absorption spectroscopy, Nat. Commun. **11**, 4042 (2020).
[8] K. S. Zinchenko, F. Ardana-Lamas, I. Seidu, S. P. Neville, J. van der Veen, V. U. Lanfaloni, M. S. Schuurman, and H. J. Wörner, Sub-7-femtosecond conical-intersection dynamics probed at the carbon K-edge, Science **371**, 489 (2021).
[9] C. S. Wang, N. E. Frattini, B. J. Chapman, S. Puri, S. M. Girvin, M. H. Devoret, and R. J. Schoelkopf, Observation of wave-packet branching through an engineered conical intersection, Phys. Rev. X **13**, 011008 (2023).
[10] C. H. Valahu *et al.*, Direct observation of geometric-phase interference in dynamics around a conical intersection, Nat. Chem. **15**, 1503 (2023).
[11] M. H. Farag, T. L. C. Jansen, and J. Knoester, Probing the interstate coupling near a conical intersection by optical spectroscopy, J. Phys. Chem. Lett. **7**, 3328 (2016).
[12] S. P. Neville, M. Chergui, A. Stolow, and M. S. Schuurman, Ultrafast X-ray spectroscopy of conical intersections, Phys. Rev. Lett. **120**, 243001 (2018).
[13] M. Kowalewski, K. Bennett, K. E. Dorfman, and S. Mukamel, Catching conical intersections in the act: Monitoring transient electronic coherences by attosecond stimulated X-ray Raman signals, Phys. Rev. Lett. **115**, 193003 (2015).
[14] D. Keefer, T. Schnappinger, R. de Vivie-Riedle, and S. Mukamel, Visualizing conical intersection passages via vibronic coherence maps generated by stimulated ultrafast X-ray Raman signals, Proc. Natl. Acad. Sci. U.S.A. **117**, 24069 (2020).
[15] D. Keefer, V. M. Freixas, H. Song, S. Tretiak, S. Fernandez-Alberti, and S. Mukamel, Monitoring molecular vibronic coherences in a bichromophoric molecule by ultrafast X-ray spectroscopy, Chem. Sci. **12**, 5286 (2021).
[16] S. M. Cavaletto, D. Keefer, and S. Mukamel, High temporal and spectral resolution of stimulated X-ray Raman signals with stochastic free-electron-laser pulses, Phys. Rev. X **11**, 011029 (2021).
[17] D. Keefer, S. M. Cavaletto, J. R. Rouxel, M. Garavelli, H. Yong, and S. Mukamel, Ultrafast X-ray probes of elementary molecular events, Annu. Rev. Phys. Chem. **74**, 73 (2023).
[18] U. Weiss, *Quantum Dissipative Systems*, 4th ed. (World Scientific, Singapore, 2012).
[19] A. Nitzan, *Chemical Dynamics in Condensed Phases* (Oxford University Press, 2006).
[20] V. May and O. Kühn, *Charge and Energy Transfer Dynamics in Molecular Systems* (Wiley-VCH, New York, 2011).
[21] J. Gilmore and R. H. McKenzie, Spin boson models for quantum decoherence of electronic excitations of biomolecules and quantum dots in a solvent, J. Phys. Condens. Matter **17**, 1735 (2005).
[22] H.-G. Duan and M. Thorwart, Quantum mechanical wave packet dynamics at a conical intersection with strong vibrational dissipation, J. Phys. Chem. Lett. **7**, 382 (2016).
[23] H.-G. Duan, R. J. D. Miller, and M. Thorwart, Impact of vibrational coherence on the quantum yield at a conical intersection, J. Phys. Chem. Lett. **7**, 3491 (2016).
[24] H.-G. Duan, V. I. Prokhorenko, R. Cogdell, K. Ashraf, A. L. Stevens, M. Thorwart, and R. J. D. Miller, Nature does not rely on long-lived electronic quantum coherence for photosynthetic energy transfer, Proc. Natl. Acad. Sci. U.S.A. **114**, 8493 (2017).
[25] H.-G. Duan, M. Thorwart, and R. J. D. Miller, Does electronic coherence enhance anticorrelated pigment vibrations under realistic conditions?, J. Chem. Phys. **151**, 114115 (2019).
[26] H.-G. Duan, A. Jha, L. Chen, V. Tiwari, R. J. Cogdell, K. Ashraf, V. I. Prokhorenko, M. Thorwart, and R. J. D. Miller, Quantum coherent energy transport in the Fenna-Matthews-Olson complex at low temperature, Proc. Natl. Acad. Sci. U.S.A. **119**, e2212630119 (2022).
[27] A. Jha, P.-P. Zhang, V. Tiwari, L. Chen, M. Thorwart, R. J. D. Miller, and H.-G. Duan, Unraveling quantum coherences mediating primary charge transfer processes in photosystem II reaction center, Sci. Adv. **10**, eadk1312 (2024).

[28] Y. Tanimura and R. Kubo, Time evolution of a quantum system in contact with a nearly Gaussian-Markoffian Noise bath, J. Phys. Soc. Jpn. **58**, 101 (1989).

[29] A. Furlan, M. J. Riley, and S. Leutwyler, The Jahn–Teller effect in triptycene, J. Chem. Phys. **96**, 7306 (1992).

[30] J. R. Johansson, P. D. Nation, and F. Nori, QuTiP2: A PYTHON framework for the dynamics of open quantum systems, Comput. Phys. Commun. **184**, 1234 (2013).

[31] N. Lambert, T. Raheja, S. Cross, P. Menczel, S. Ahmed, A. Pitchford, D. Burgarth, and F. Nori, QuTiP-BoFiN: A bosonic and fermionic numerical hierarchical-equations-of-motion library with applications in light-harvesting, quantum control, and single-molecule electronics, Phys. Rev. Res. **5**, 013181 (2023).

[32] A. Garg, J. N. Onuchic, and V. Ambegaokar, Effect of friction on electron transfer in biomolecules, J. Chem. Phys. **83**, 4491 (1985).

[33] R. Trebino, K. W. DeLong, D. N. Fittinghoff, J. N. Sweetser, M. A. Krumbügel, B. A. Richman, and D. J. Kane, Measuring ultrashort laser pulses in the time-frequency domain using frequency-resolved optical gating, Rev. Sci. Instrum. **68**, 3277 (1997).

[34] See Supplemental Material at http://link.aps.org/supplemental/10.1103/PhysRevLett.133.098001 for the detailed stick spectrum related to the transition around 250 cm^{-1} as seen in Fig. 4.

[35] S. M. Cavaletto, D. Keefer, and S. Mukamel, High temporal and spectral resolution of stimulated X-ray Raman signals with stochastic free-electron-laser pulses, Phys. Rev. X **11**, 011029 (2021).

[36] W. Hu, I. Gustin, T. D. Krauss, and I. Franco, Tuning and enhancing quantum coherence time scales in molecules via light-matter hybridization, J. Phys. Chem. Lett. **13**, 11503 (2022).

[37] M. Rivera, L. Stojanović, and R. Crespo-Otero, Role of conical intersections on the efficiency of fluorescent organic molecular crystals, J. Phys. Chem. A **125**, 1012 (2021).

Supplemental Material to Coherent ultrafast stimulated x-ray Raman spectroscopy of dissipative conical intersections

Florian Otterpohl,[1] Daniel Keefer,[2] Shaul Mukamel,[3] and Michael Thorwart[1,4]

[1] *I. Institut für Theoretische Physik, Universität Hamburg, Notkestr. 9, 22607 Hamburg, Germany*
[2] *Max-Planck-Institut für Polymerforschung, 55128 Mainz, Germany*
[3] *Department of Chemistry, University of California, Irvine, California 92614, USA*
[4] *The Hamburg Center for Ultrafast Imaging, Luruper Chaussee 149, 22761 Hamburg, Germany*

(Dated: April 8, 2024)

In this Supplemental Material, we provide further information on the transition around 250 cm^{-1} as seen in Fig. 4 of the main text.

Consider the undamped Hamiltonian

$$H = H_{\mathrm{el}} + H_{\text{el-nuc}} + H_{\mathrm{nuc}} \tag{S1}$$

with the parameters given in the main text. We refer to the energy eigenbasis of this Hamiltonian with energies E_k and states $|k\rangle$ as the vibronic basis. The basis consisting of the uncoupled electronic and vibrational states $|e/g, n_t, n_c\rangle$ is referred to as product basis where $|e/g\rangle$ refers to the electronic excited/ground state and $|n_{c/t}\rangle$ refers to the occupation number of the coupling/tuning mode. The stick height $|\mu_{k,l}|^2$ as shown in Fig. 4 of the main text is obtained from

$$\mu_{k,l} = \sum_{n_t,n_c} [\langle k|g, n_t, n_c\rangle \langle e, n_t, n_c|l\rangle + \langle k|e, n_t, n_c\rangle \langle g, n_t, n_c|l\rangle]. \tag{S2}$$

In analogy to the blue curve in Fig. 2c) of the main text, the dynamics of $\langle\sigma_z(t)\rangle$ is given in Fig. S1. The transition

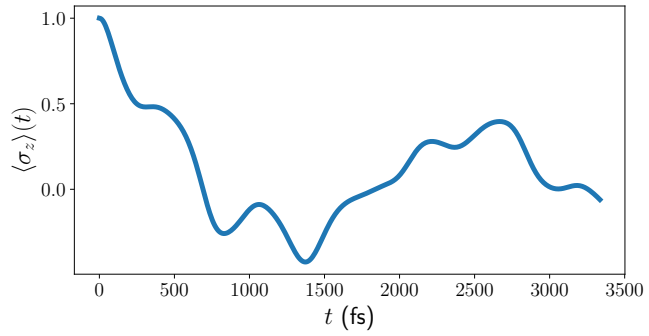

FIG. S1. Time evolution of $\langle\sigma_z(t)\rangle$ for the undamped case.

belonging to $E_1 - E_0 = 241.5\mathrm{cm}^{-1}$ is the transition with the second largest stick height in Fig. 4 of the main text. The overlaps of the vibronic states $|0\rangle$ and $|1\rangle$ with a range of product states are shown in Fig. S2 and Fig. S3 respectively. As room temperature corresponds to a wave number of roughly 200 cm^{-1}, which is similar to the oscillator wavenumbers of $\Omega = 300$ cm^{-1}, the two lowest eigenstates of the oscillators will be populated and as seen

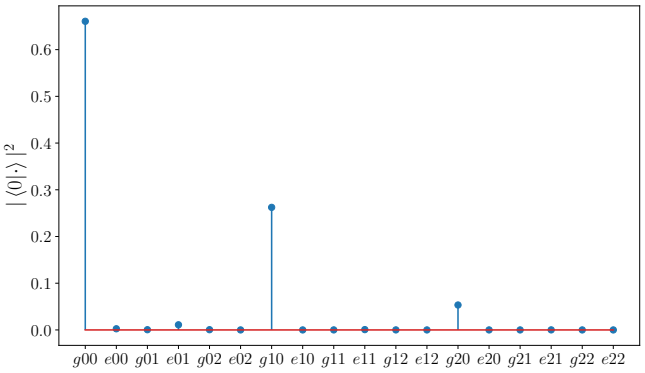

FIG. S2. Overlap between vibronic eigenstate $|0\rangle$ and each product state indicated on x-axis.

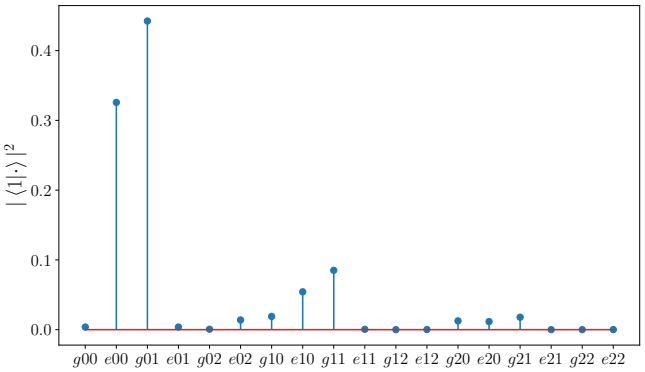

FIG. S3. Overlap between vibronic eigenstate $|1\rangle$ and each product state indicated on x-axis.

from Fig. S1, both electronic states are also populated most of the time. Thus, the states $|0\rangle$ and $|1\rangle$ are also populated.